# Multiscale Computational Framework to Investigate Integrin Mechanosensing and Cell Adhesion

Andre R. Montes,[1] Gabriela Gutierrez,[1] Adrian Buganza Tepole,[2, a)] and Mohammad R.K. Mofrad[1, b)]

[1)] *Department of Mechanical Engineering, University of California, Berkeley, CA*

[2)] *School of Mechanical Engineering, Purdue University, West Lafayette, IN*

(*Electronic mail: abuganza@purdue.edu, mofrad@berkeley.edu)

(Dated: 24 March 2023)

[a)] Tepole Mechanics & Mechanobiology Lab: engineering.purdue.edu/tepolelab/

[b)] Molecular Cell Biomechanics Lab: biomechanics.berkeley.edu

## ABSTRACT

Integrin mechanosensing plays an instrumental role in cell behavior, phenotype, and fate by transmitting mechanical signals that trigger downstream molecular and cellular changes. For instance, force transfer along key amino acid residues can mediate cell adhesion. Disrupting key binding sites within $\alpha_5\beta_1$ integrin's binding partner, fibronectin (FN) diminishes adhesive strength. While past studies have shown the importance of these residues in cell adhesion, the relationship between the dynamics of these residues and how integrin distributes force across the cell surface remains less explored. Here, we present a multiscale mechanical model to investigate the mechanical coupling between integrin nanoscale dynamics and whole-cell adhesion mechanics. Our framework leverages molecular dynamics simulations to investigate residues within $\alpha_5\beta_1$-FN during stretching and the finite element method to visualize the whole-cell adhesion mechanics. The forces per integrin across the cell surface of the whole-cell model were consistent with past atomic force microscopy and Förster resonance energy transfer measurements from literature. The molecular dynamics simulations also confirmed past studies that implicate two key sites within FN that maintain cell adhesion: the synergy site and RGD motif. Our study contributed to our understanding of molecular mechanisms by which these sites collaborate to mediate whole-cell integrin adhesion dynamics. Specifically, we showed how FN unfolding, residue binding/unbinding, and molecular structure contribute to $\alpha_5\beta_1$-FN's nonlinear force-extension behavior during stretching. Our computational framework could be used to explain how the dynamics of key residues influence cell differentiation or how uniquely designed protein structures could dynamically limit the spread of metastatic cells.


## I. INTRODUCTION

Cell-matrix junctions, governed in part by macromolecular structures known as focal adhesions (FAs), can alter cell phenotype, behavior, and fate via applied mechanical signals that trigger downstream molecular and cellular changes[1–9]. At the heart of FA formation is a transmembrane heterodimer known as integrin containing $\alpha$- and $\beta$- subunits. Normally, nascent FAs initiate with integrin activation, where cytoplasmic proteins bind to the integrin tails and the integrin head extends to an active state with a higher affinity for ligand binding[2,10]. However, the activation of a particular integrin, $\alpha_5\beta_1$ appears to follow a separate mechanism where an extended conformation

may not be required to bind to its primary ligand, fibronectin (FN)[11,12]. Instead, $\alpha_5\beta_1$ binds to FN before cytoplasmic proteins anchor it to the cytoskeleton and additional integrins cluster together to create a mature FA (Fig. 1A).

The connection between $\alpha_5\beta_1$ integrin and FN is a main mechanosensing unit for external forces transmitting along amino acid residues that mediate cell adhesion[12]. The two principal $\alpha_5\beta_1$ binding sites in FN include the 8-amino-acid-long DRVPHSRN synergy site and the RGD motif[12–14]. Upon mutation of R1374 and R1379 within the synergy site, spinning disk assays showed a reduction in cell-substrate adhesion strength; moreover, a perturbation of FN's RGD motif inhibited adhesion altogether[15]. While the synergy site and RGD motif have been shown to a play a role in cell adhesion, their nanoscale dynamics and force transduction pathway are less resolved. Elucidating how these residues maintain cell adhesion during integrin mechanosensing is important because their nanomechanics could be leveraged to control cell phenotype or motility.

Notably, $\alpha_5\beta_1$ predominant role in mediating cell adhesion lends itself to be instrumental in the progression of various pathologies. For example, imposing a fibrotic microenvironment on cells by depositing collagen-I or applying biomechanical forces to the cancer cells leads to greater $\alpha_5\beta_1$ integrin-mediated proliferation[16,17]. Similarly, as a tumor's rigidity increases, mechanosensitive $\alpha_5\beta_1$ integrins are recruited and cluster together, creating larger FAs and stress fibers that promote tumor growth via a positive biochemical and biophysical feedback loop[18,19]. By understanding the link between nano and micromechanics of the cell, we could influence differentiation or mitigate the uncontrolled spread of metastatic cells through targeted protein or drug design.

Therefore, to uncover the mechanical coupling between the nanoscale dynamics of key residues in $\alpha_5\beta_1$ integrin and whole-cell adhesion dynamics, we built a multiscale model. Specifically, we combined adhesion kinetics, the finite element (FE) method, and molecular dynamics (MD) to demonstrate how key residues contributed to spring-like force-extension behavior which in turn influenced the whole-cell spatial distribution of forces on integrins (Fig. 1B). The force per integrin results from our model were within those measured by past atomic force microscopy (AFM)[20] and Förster resonance energy transfer (FRET) measurements[21]. The model indicated localization of $\alpha_5\beta_1$ integrin along the cell periphery, which is consistent with cell-based studies that stain for $\beta_1$ integrin and FN fragments[22]. Most importantly, the model contributed an inside look at the molecular dynamics by which the DRVPHSRN synergy site and RGD motif work together to mediate whole-cell adhesion mechanics.

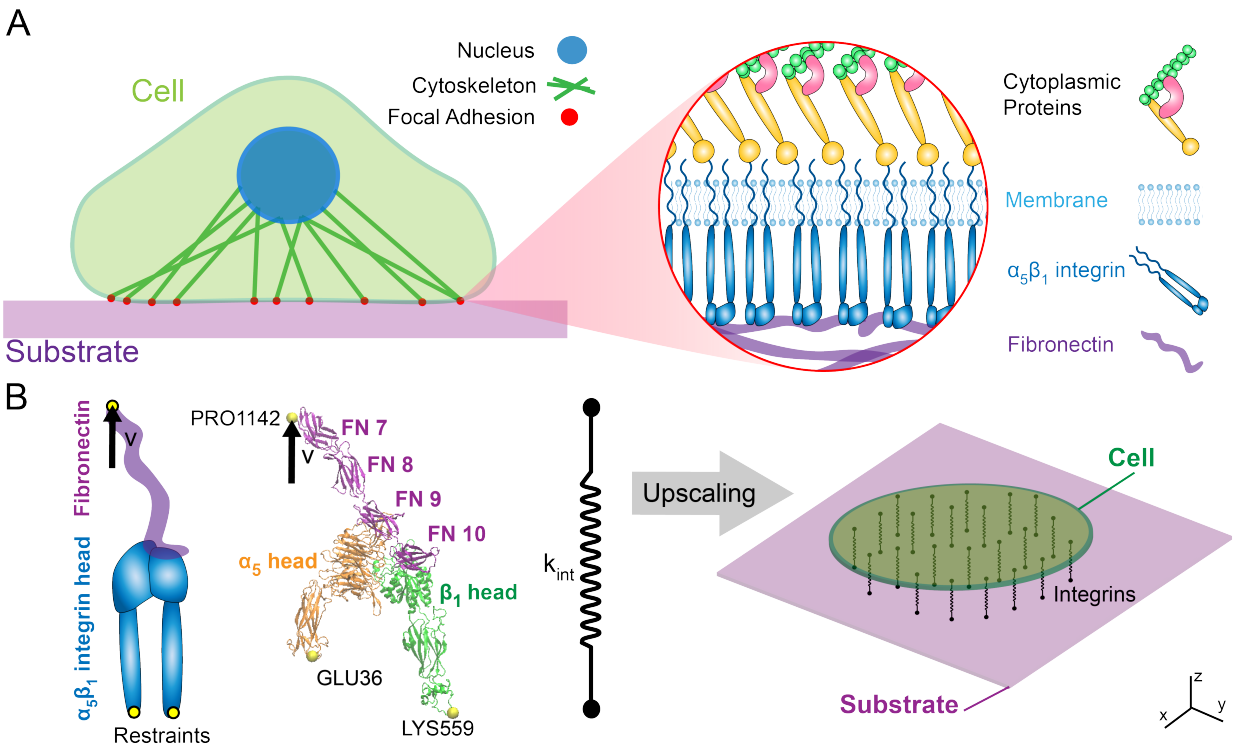


FIG. 1. Simplified schematic of multiscale cell mechanobiology within cell adhesion mediated by $\alpha_5\beta_1$ integrin (A) The cell attaches to a substrate via FAs which house multiple biomolecules including cytoplasmic proteins that anchor integrins to corresponding ligands. (B) The molecular assembly consisted of $\alpha_5\beta_1$ integrin head bound to fibronectin type III fragment 7-10. For the MD simulations, restraints were placed on GLU36 and LYS559 with an applied velocity at PRO1142. The $\alpha_5\beta_1$-FN's stretching behavior was characterized by a spring that was applied to a 2D continuum model of an elastic cell on a substrate.

## II. METHODS

### A. All-atom Steered Molecular Dynamics

The 7NWL.pdb file containing human $\alpha_5\beta_1$ integrin in complex with FN and TS2/16 Fv-clasp was downloaded from the Protein Data Bank[12]. Schumacher et al. used the TS2/16 Fv-clasp to aid in the crystallization of $\alpha_5\beta_1$-FN and is not naturally occurring and was therefore removed using PyMOL 2.5[23], leaving three protein chains to be analyzed as part of the remaining complex: $\alpha_5$ integrin, $\beta_1$ integrin, and FN type III. We refer to this complex, or system as "$\alpha_5\beta_1$-FN."

All-atom molecular dynamics (MD) simulations were run in GROMACS 2018.3[24] with the AMBER99SB-ildn force field and periodic boundary conditions. Using the Gromacs built-in func-

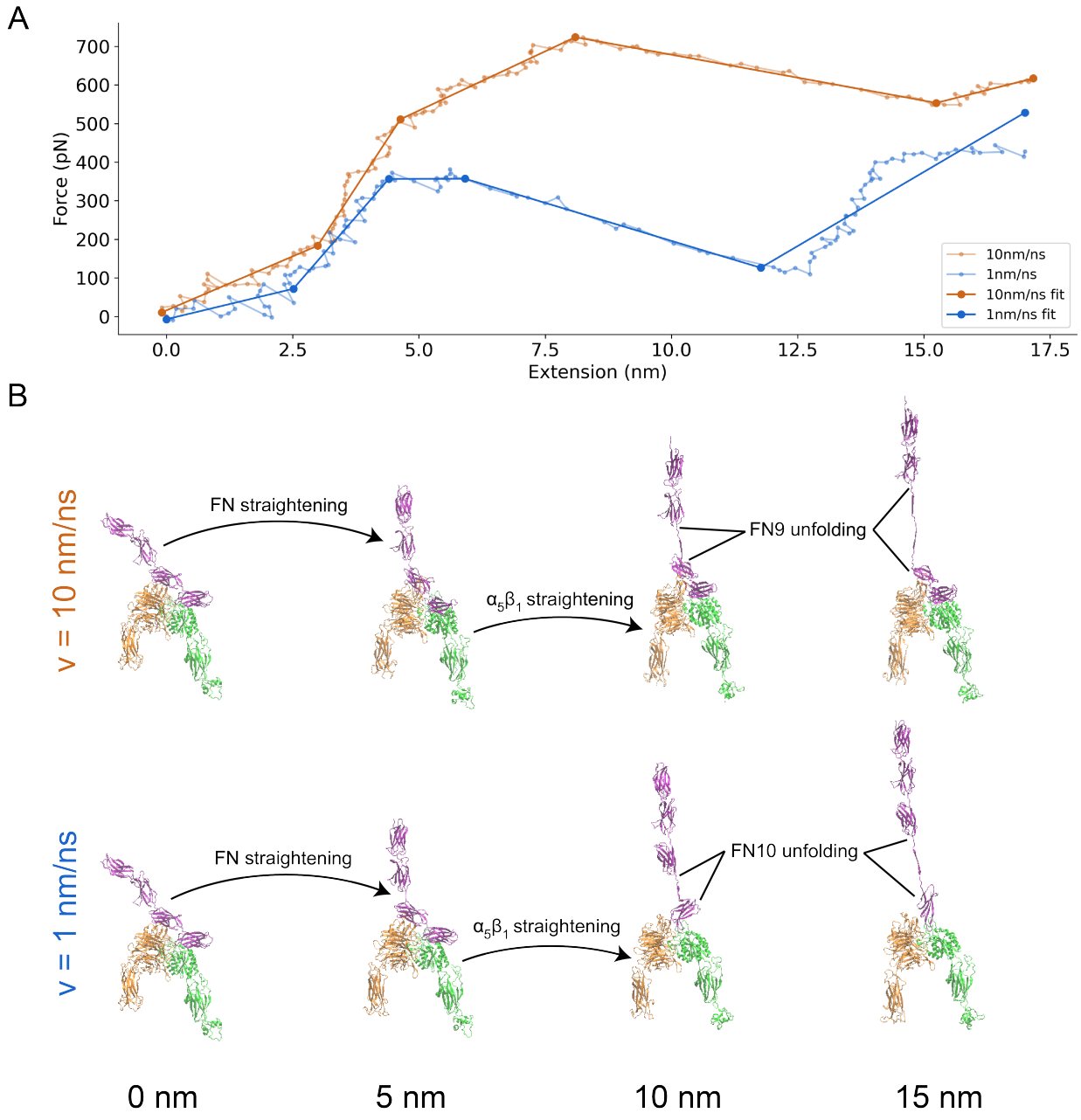


FIG. 2. (A) Force-extension curve of $\alpha_5\beta_1$-FN stretching at 10 and 1 nm/ns. The raw data are shown in transparent solid lines and the 5-segment piecewise linear fits are shown in opaque solid lines. (B) Frames of $\alpha_5\beta_1$-FN during extension at 10 nm/ns and 1 nm/ns showing distinct stretching configurations at 0, 5, 10, and 15 nm of extension. In both cases, FN and $\alpha_5\beta_1$ straightened before FN unfolded. However, for the 10 nm/ns case, the FN9 subdomain unfolded. Whereas for the 1 nm/ns case, FN10 unfolded. Movies showing $\alpha_5\beta_1$-FN extension can be found in the Supplementary Materials.

tion, `gmx editconf`, we rotated the $\alpha_5\beta_1$-FN complex 45 degrees to align the structure inside a

18nm x 45nm x 19nm box. The structure was solvated in a TIP3P water box with 0.15mM NaCl resulting in a system with 1.5 million atoms.

The energy minimization step was carried out for 15k steps utilizing the steepest gradient descent algorithm with a step size of 0.005nm. Energy over time was extracted using the `gmx energy` command and then plotted in Python. The structure was then equilibrated using a sequential 1ns NVT followed by a 10ns NPT simulation with H-bonds restrained. For the NVT simulation, we used Nose-Hoover temperature coupling at 310K. For the NPT simulation, Parrinello-Rahman pressure coupling at 1 bar was added. After the equilibration runs were completed, we extracted and plotted the root-mean-square deviation (RMSD), temperature, and pressure to confirm system stability.

Upon verifying system equilibration, we ran two steered MD simulations. The positions of Lysine (LYS) 559 and glutamic acid (GLU) 36 at the proximal ends of the integrin headpieces were restrained using the `gmx genrestr` command (Fig. 1B). Proline (PRO) 1142 at the distal end of the FN chain was pulled vertically at 1 and 10 nm/ns using a 50kJ/mol/nm spring with an umbrella potential for 25 and 3 ns, respectively. Constant force simulations were ran with veritcal pulling forces of 300 and 500 pN on PRO1142. The timestep for all steered MD simulations was 2fs. The Molecular Dynamics Parameter (.mdp) files for running the energy minimization, equilibration, and steered MD can be found in the Supplementary Materials.

## B. Force Distribution Analysis

Protein structures and MD simulation trajectories were visualized in Visual Molecular Dynamics (VMD) 1.9.4a[25]. We then used the Time-Resolved Force Distribution Analysis (FDA) software package, gromacs-fda (available: `https://github.com/HITS-MBM/gromacs-fda`) with Gromacs 2020.4 to calculate the punctual stresses at each of the residues along the $\alpha_5$ and $\beta_1$ integrin chains, as well as FN. The punctual stress is the sum of absolute values of scalar pairwise forces exerted on each residue. The parameter settings for the FDA can be found in the Supplementary Materials. The gromacs-fda-vmd plugin overlaid the punctual stress heatmap onto the protein renderings in VMD. Areas of interest for the FDA were the DRVPHSRN synergy site and RGD motif/loop (Fig. 3).

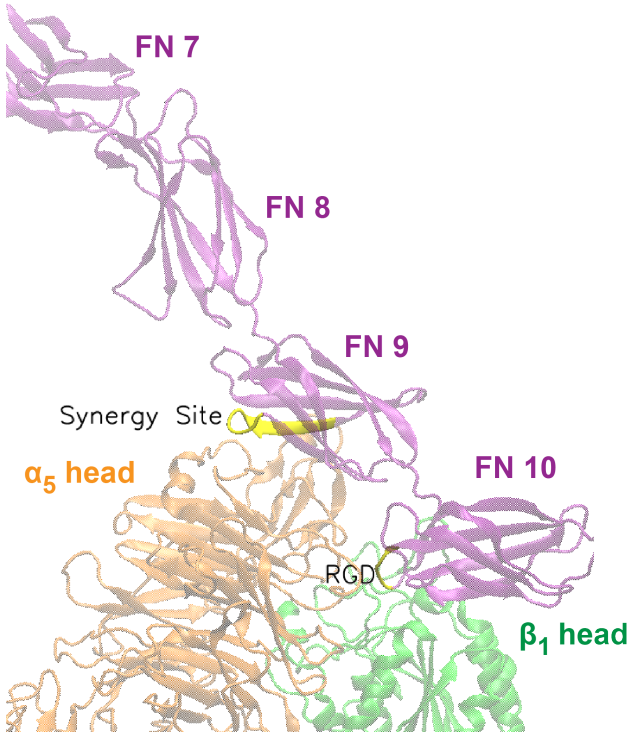


FIG. 3. Close up view of DRVPHSRN synergy site and RGD motif/loop (shown in yellow) in FN that interact with the $\alpha_5$ and $\beta_1$ heads, respectively.

## C. Whole-Cell Finite Element Model

The custom finite element (FE) model represented the cell as a thin elastic disk on top of an elastic substrate. The cell surface was assumed to be a neo-Hookean[26] constitutive material model.

$$\sigma_{\mathbf{s}}^{\mathbf{pas}} = \mu_s \mathbf{b_s} - p_s \mathbf{I}, \tag{1}$$

$$\sigma_{\mathbf{c}}^{\mathbf{pas}} = \mu_c \mathbf{b_c} - p_c \mathbf{I}, \tag{2}$$

where $\sigma_{\mathbf{s}}^{\mathbf{pas}}$ and $\sigma_{\mathbf{c}}^{\mathbf{pas}}$ are the passive substrate and cell stress respectively. The shear moduli are denoted $\mu_s$, $\mu_c$. The deformation is characterized by the left Cauchy-Green tensors $\mathbf{b_s}$, $\mathbf{b_c}$. The pressures $p_s, p_c$ are computed from boundary conditions, in this case for plane stress. To account for cell contractility, an active stress field was applied inside the cell,

$$\sigma_{\mathbf{c}}^{\mathbf{act}} = t_{myo} \mathbf{I}, \tag{3}$$

where $\sigma_{\mathbf{c}}^{\mathbf{act}}$ is the active cell stress due to the applied actin-myosin traction, $t_{myo}$ (Pa):

$$t_{myo} = \begin{cases} 100t & 0 < t < 2 \\ 200 & 2 \leq t \leq 12 \end{cases} \tag{4}$$

where $t$ is the simulation time. We used a previously developed catch-slip bond model of adhesion to determine the number of integrin-substrate bonds per node in the FE mesh in a force dependent manner[27,28]. This model assumes that the $\alpha_5\beta_1$-FN complexes behave as parallel springs that connect and disconnect to the substrate based on an association constant, $K_{on}$ and on a force dependent dissociation constant, $K_{off}$, respectively.

$$K_{off} = K_a e^{\frac{f_{int}}{F_a}} + K_b e^{-\frac{f_{int}}{F_b}} , \tag{5}$$

where $K_a$, $F_a$, $K_b$, and $F_b$ are fitted parameters and $f_{int}$ is the magnitude of the force per $\alpha_5\beta_1$-FN. The force vector per integrin bond, ($\mathbf{f_{int}}$), is computed per node and is related to the fraction (concentration) of $\alpha_5\beta_1$-FN bonds $C$ with respect to the maximum density $\rho_{i,max}$, the local area of the adhesion $A$ (area per node of the FE mesh), the $\alpha_5\beta_1$-FN spring constant $k_{int}$, and the spring extension $\mathbf{u_{int}}$ at that node,

$$\mathbf{f_{int}} = C\rho_{i_{max}} A k_{int} \mathbf{u_{int}} . \tag{6}$$

The fraction of $\alpha_5\beta_1$-FN bonds $C$ needs to be updated in time. For a given node,$i$ given the previous value of the bond concentration, $C$, the updated bond concentration $C_{t+\Delta t}$ at each subsequent time step is based on the update

$$C_{t+\Delta t} = C(1 - K_{off}\Delta t) + K_{on}\Delta t(1 - C) . \tag{7}$$

Note that the update eq. (7) is based on treating the bond kinetics in the limit of an ordinary differential equation discretized in time with an explicit Euler scheme.

With all phenomena taken together, the elastodynamic equations for the cell and substrate include elastic deformation of the cell ($\sigma_{\mathbf{c}}^{\mathbf{pas}}$), active contractile stress within the cell ($\sigma_{\mathbf{c}}^{\mathbf{act}}$), and elastic deformation of the substrate ($\sigma_{\mathbf{s}}^{\mathbf{pas}}$):

$$\mathbf{f}_{c,ext} - \nabla \cdot \sigma_{\mathbf{c}} = \rho_c \mathbf{a}_c \tag{8}$$

$$\mathbf{f}_{s,ext} - \nabla \cdot \sigma_{\mathbf{s}} = \rho_s \mathbf{a}_s \tag{9}$$

where $\sigma_{\mathbf{c}} = \sigma_{\mathbf{c}}^{\mathbf{pas}} + \sigma_{\mathbf{c}}^{\mathbf{act}}$ is the total stress in the cell, $\sigma_{\mathbf{s}} = \sigma_{\mathbf{s}}^{\mathbf{pas}} + \sigma_{\mathbf{s}}^{\mathbf{act}}$ is the total stress in the substrate, $\mathbf{f}_{c,ext}, \mathbf{f}_{s,ext}$ are the external forces acting in either the cell or the substrate, $\rho_c$, $\rho_s$ are the

densities of cell and substrate respectively (assigned to that of water), and $\mathbf{a}_c, \mathbf{a}_s$ the corresponding accelerations. The external forces for the substrate are those from the integrin bonds $\mathbf{f_{int}}$ plus a small drag component to dissipate oscillations over time. For the cell, external forces include the opposite forces from the integrin-bonds, $-\mathbf{f_{int}}$, and additional contributions for regularization of the cell deformation, namely a small drag dissipation, bending regularization at the mesh boundary, a random fluctuation due to actin polymerization also at the boundary, and an area constraint that acts as an internal pressure.

The strong form of the elastodynamic equations 8 and 9 are not directly evaluated. Instead, internal forces are computed through the weak form:

$$\int \sigma : \delta \mathbf{d} \tag{10}$$

where the $\delta \mathbf{d}$ is the variation of the symmetric velocity gradient, i.e. virtual work by moving each node by an independent variation $\delta u$. The explicit mid-point rule was used for time integration of the second order system of equations.

The $\alpha_5\beta_1$-FN complex within the FE model was modeled as a nonlinear spring applying piecewise linear interpolation in Python to the force-extension curves provided by the MD simulations. A dynamic explicit mesh generator, El Topo[29], created and maintained the mesh during the simulation run. Three $\alpha_5\beta_1$-FN stiffness values ($k_{int}$) were used: 1pN/nm, 31pN/nm, and variable stiffnesses extracted from the MD simulation force-extension curves. Settings for each simulation run can be found in Supplementary Materials.

## D. Multiscale Model Coupling

The Gromacs function `mdrun` output the force on the $\alpha_5\beta_1$-FN complex. Furthermore, `gmx trajectory` was used to extract the center-of-mass coordinates of the restraints, LYS559 and GLU36, as well as the pull residue, PRO1142. The $\alpha_5\beta_1$-FN extension length was measured in Python as the average vertical distance between PRO1142 and each of the two restrained residues. The resulting force-extension curve for each simulation run was then plotted. The `optimize` function from the `SciPy` library was used to produce a 5-segment piecewise linear fit on the 1 and 10 nm/ns force-extension curves, respectively. Ultimately, the 1 nm/ns curve-fit was used as a variable displacement-dependent spring constant in the whole-cell model to make up the "MD-driven" $\alpha_5\beta_1$-FN stiffness, $k_{int}$.

## III. RESULTS AND DISCUSSION

### A. $\alpha_5\beta_1$-FN exhibited nonlinear and rate dependent stretching behavior under applied constant velocity

Prior to running the steered MD simulations at two pulling rates, the model's energy minimized to -1.37e7 kJ/mol and the RMSD of the system plateaued while the pressure and temperature also remained stable during the NPT simulation (Supplementary Material). We chose 1 and 10 nm/ns pull rates for the steered MD simulations based on similar rates in other integrin subtypes[30,31]. As expected, $\alpha_5\beta_1$-FN exhibited rate-dependent stretching behavior, meaning that the $\alpha_5\beta_1$-FN force-displacement curves varied by pull rate (Fig. 2 A). The 10 nm/ns simulation reached a higher peak force of 723 pN and greater initial slope of 56 pN/nm compared to 444 pN and 31 pN/nm, respectively for the 1 nm/ns simulation.

In both cases, the stretching was dominated by FN, while integrin remained mostly rigid with some minor rotation and straightening. Curiously, at the faster 10 nm/ns pull rate, FN9 unraveled first before unbinding from the $\alpha_5$ head at the synergy site, whereas limited unraveling of FN was observed prior to unbinding for the slower 1 nm/ns pull rate (Fig. 2 B). Following the disconnection between FN and $\alpha_5$ at the synergy site, the force on the whole $\alpha_5\beta_1$ integrin head became biased towards the RGD motif, causing the integrin heads to straighten with the elongation of $\beta_1$.

The observed viscoelastic behavior of $\alpha_5\beta_1$ has been shown both experimentally and computationally. Single-molecule AFM studies show higher rupture forces at faster pull rates[20] and separate steered MD simulations of integrin[30,31] and FN[32] showed rate-dependent and force-dependent stretching behavior seen in viscoelastic materials. We expected this viscoelastic behavior to remain when $\alpha_5\beta_1$ and FN are in complex. To confirm, we tested $\alpha_5\beta_1$-FN's viscoelasticity *in silico* via constant force simulations at 300 and 500 pN, similar to what would be done in a mechanical creep test where constant stress is applied (Fig. 4). We fit the Bausch viscoelasticity model, which combines a Kelvin model with a dashpot in series[33], to the extension-time plots, supporting the characterization of $\alpha_5\beta_1$-FN's time-dependent stretching and viscoelastic nature.

While our MD simulations and previous literature have demonstrated the nonlinear stretching behavior of $\alpha_5\beta_1$-FN, multiscale models assume a linear integrin stiffness between 0.001-2 pN/nm[27,28,34]. Recent multiscale models have used this assumption when analyzing fundamental phenomena such as integrin activation, organization, and clustering at the cell and tissue

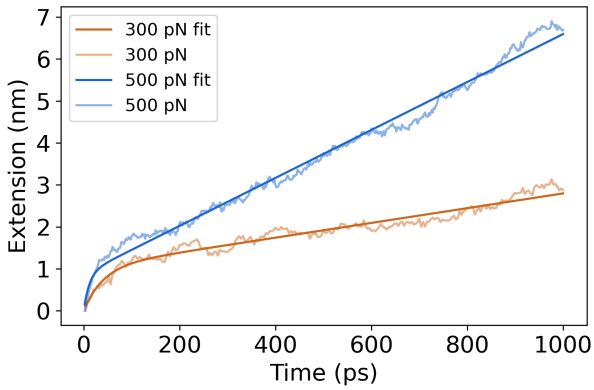


FIG. 4. Extension plots of constant force simulations at 300pN and 500pN pulling forces. The Bausch[33] viscoelastic model was fit to each of the plots.

scales[27,28,34]. Most recently, Guo et al. showed a framework that combined adhesion kinetics with the finite element method (FEM) to model stretch-driven mechanosensing at the tissue level by coupling integrin adhesion with the nonlinear tissue mechanics of fibrin and collagen[27]. While these models provide unique insights into multiscale mechanobiology of cell adhesion, for models to account for integrin and FN's nonlinear stretching behavior, a dynamic spring stiffness that adjusts depending on extension is required. For our work, we used our steered MD force-extension plots to inform a dynamically changing spring in a continuum model of the whole cell.

A limitation of our approach is that MD simulations are computationally expensive and runtimes would be unreasonably long if we adopted experimentally relevant 800 nm/s pull rates used by past AFM studies[35,36]. However, using faster pull rates leads to higher single-molecule forces beyond 300pN as was noticed in our force-extension curves. Previous studies found average *in situ* rupture forces for $\alpha_5\beta_1$-FN to be 34[35] and 38.6 pN[36] in endothelial cells and cardiomyocytes, respectively. Single molecule AFM conducted by Li et al. measured a mean rupture force of $\alpha_5\beta_1$-FN of 69 pN at a loading rate of 1800-2000 pN/s, with a peak rupture force of 120 pN at 18,000 pN/s[20]. More recently, FRET-based sensors were used to measure adhesion forces between 1-7 pN on fibroblasts plated on glass[21]. All these measured forces are much lower than those predicted by the MD simulations. Higher forces at much faster pull rates meant that our $\alpha_5\beta_1$-FN stiffness results were significantly larger than what has been observed *in vitro*. However, in all the experiments, the nonlinearity of $\alpha_5\beta_1$-FN's stretching behavior was apparent, challenging the linear stiffness assumption made by previous models[27,28,34]. Furthermore, while an average FN stiffness of 0.5 pN/nm has been reported[37,38], the coupled $\alpha_5\beta_1$-FN stiffness has not. Additionally, our

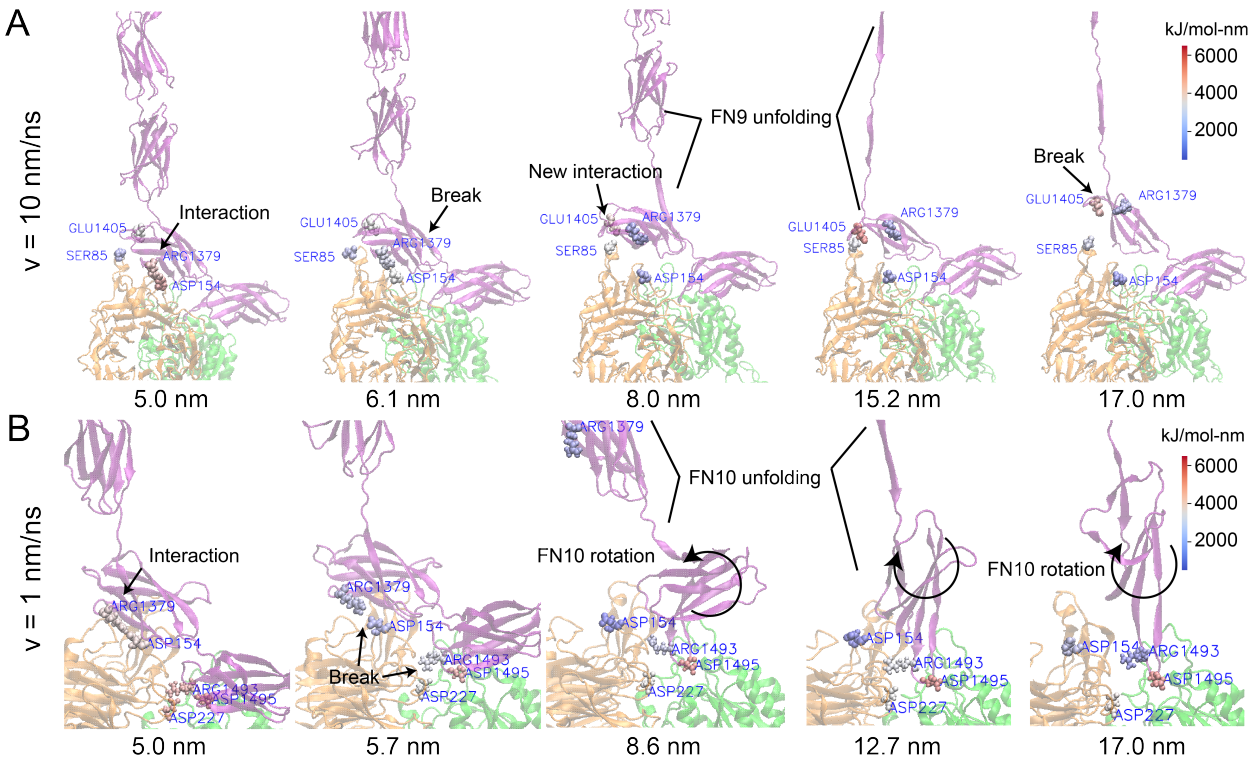


FIG. 5. Force Distribution Analysis of $\alpha_5\beta_1$-FN for two pull rates at key events. The color map refers to the punctual stress (in kJ/mol-nm) at each residue. (A) At 10 nm/ns, there was a coulombic interaction at the ARG1379-ASP154 salt bridge and no interaction between GLU1405 and SER85. As FN was extended, the salt bridge ruptured and allowed FN to rotate and establish a new interaction between GLU1405 and SER85. FN9 continued to unfold, increasing stress on the GLU1405-SER85 connection, eventually breaking it. (B) At 1 nm/ns, the ARG1379-ASP154 salt bridge, part of the synergy site, together with ARG1493 and ARG1495, part of the RGD motif, maintained a hold on FN. As FN extended, increased stress led to the simultaneous rupture of ARG1493-ASP227 and ARG1379-ASP154. This allowed FN10 to unfold and rotate. ARG1493-ASP227 disconnected and reconnected throughout the remainder of the simulation. Movies showing the FDA can be found in the Supplementary Materials.

steered MD simulations provided atomic level details that helped explain how key binding sites contributed to pull rate dependent nonlinear stretching.

## B. Force Distribution Analysis of $\alpha_5\beta_1$-FN reveals dynamics of adhesion-mediating residues that contribute to nonlinear force-extension behavior

Visualization of the coulombic interactions via Force Distribution Analysis of the steered MD results demonstrated how key adhesion mediators could contribute to nonlinear, rate-dependent, force-extension of $\alpha_5\beta_1$-FN. Two key mediators are the DRVPHSRN synergy site and the RGD motif in FN (Fig. 3). In our system, the FN synergy site was represented by residues 1373 to 1380 and the RGD motif was represented by residues 1493 to 1495. Spinning disk microscopy has previously shown that mutating one to two select residues on the synergy site leads to a decrease in overall cell adhesion and mutating the RGD motif eliminates cell adhesion force completely[15]. Furthermore, inducing a synergy site mutation or an RGD deletion leads to a reduction in single molecule rupture force of $\alpha_5\beta_1$-FN[20]. Therefore, we looked closely at the dynamics of these adhesion mediators during $\alpha_5\beta_1$-FN stretching at 1 nm/ns and 10 nm/ns.

Interestingly, the $\alpha_5\beta_1$-FN extension showed two modes of stretching depending on the pull rate. Heatmaps overlaid on the molecule illustrated the degree of coulombic interaction, where "hotter" or "redder" zones indicated larger pairwise punctual stresses. For the 10 nm/ns case, the salt bridge between arginine (ARG) 1379 and aspartic acid (ASP) 154 is broken after 6.1 nm of $\alpha_5\beta_1$-FN extension (Fig. 5A). This action then loosens the grip between $\alpha_5$ and FN9, allowing FN9 to rotate to find a new interaction between glutamic acid (GLU) 1405 and serine (SER) 85. FN9 then unfolded, contributing to the initial decrease in force and most of the extension before GLU1405 and SER85 release. Between 0 and 5 nm, FN began to straighten while simultaneously tugging on the on the synergy site and RGD. The force-extension response "softened" as the salt bridge was broken and FN9 started to rotate. The large extension and reduction in force past 8 nm (Fig. 2) was due to the rapid unfolding of FN8 while GLU1405-SER85 pinned FN9 in place. After two strands of FN8 are unwound, the applied load became directed at the GLU1405-SER85 pin until it finally separated. Notably, the unfolding pathway with two strands unwound of FN9 has been illustrated before in constant force simulations of FN[32]. Our model corroborates these results while providing new insight into the dynamics of FN unfolding when interacting with $\alpha_5\beta_1$ integrin.

The observed unbinding and unfolding sequence in $\alpha_5\beta_1$-FN was not preserved at 1 nm/ns. The salt bridges, ARG1379-ASP154 and ARG1493-ASP227 simultaneously broke at 5.7 nm of extension after a short force plateau between 4.8-5.7nm, but unlike in the 10nm/ns run, FN9 did

not create a new interaction with $\alpha_5$ (Fig. 5B). Rather, FN10 unfolded, leading to the majority of the overall extension and reduction in force from 5.7-12.7nm (Fig. 2A). During FN10 unfolding, the interaction between ARG1493 in FN and ASP227 in $\alpha_5$ alternated between high and low coulombic interactions while ARG1495 maintained adhesion with $\beta_1$ integrin. Due to the lack of interaction between the synergy site in FN9 and $\alpha_5$, FN9 was free to separate from integrin so FN10 could readily unfold. Once one strand had completely unfolded, due to the direction of the pulling force with respect to the orientation of FN10, the force needed to rotate FN10 prior to unwinding the second strand, which led to an increase in force (Fig. 2B).

At both pull rates, the synergy site and RGD loop played key roles in maintaining the adhesion between $\alpha_5\beta_1$ and FN. Specifically, the salt bridge between ARG1379 and ASP154 contributed to the molecule's initial "stiff" behavior prior to FN unfolding; and part of the RGD loop between $\beta_1$ and FN10 was the only remaining connection between integrin and FN after full extension. Due to their instrumental role, it stands to reason that interfering with these residues via point mutations would reduce adhesion[15] and rupture force[20]. While measured *in vitro* forces on $\alpha_5\beta_1$-FN have been shown to be much smaller than we have presented due to our model's much faster pulling speed, nonlinear force-extension behavior and rapid jumps in force have been observed[15,20,21]. We showed how key residues could contribute to this characteristic behavior during $\alpha_5\beta_1$-FN extension in a pull rate dependent manner. To bridge the nanoscale integrin stretching to cell-scale integrin dynamics, as a proof-of-concept, we modeled the force-extension of $\alpha_5\beta_1$ as a nonlinear spring and used it to scale up to a 2D whole-cell continuum model.

### C. Multiscale integration of $\alpha_5\beta_1$-FN force-extension with whole-cell integrin dynamics

Prior to integrating the force-extension curves from the MD runs, we had ran a baseline simulation of the whole-cell model with similar parameters to those commonly used in literature[27,28,34]. In particular, we set the $\alpha_5\beta_1$-FN stiffness, $k_{int}$, to 1pN/nm. For all simulations, the cell contractility was ramped from 0 to 200Pa within the first 2s and held at 200Pa for the remainder of the 12s simulation. Integrins were recruited to the cell border, achieving maximum concentration and force as the contractility reached 200Pa at 2s (Fig. 6).

Integrin's spatial distribution on the cell's leading edge during motion has been previously observed *in vitro*[22], corroborating the results from the model (Fig. 7A). However, the model's force values during the progressive contraction reached an average peak of 60.9pN (Fig. 7B)

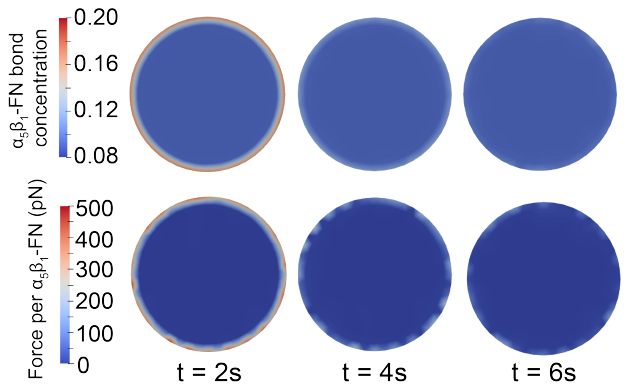


FIG. 6. $\alpha_5\beta_1$-FN bond concentration (top) and force per $\alpha_5\beta_1$-FN (bottom) results for the baseline whole-cell simulation with $k_{int} = 1$pN/nm. $\alpha_5\beta_1$-FN localization and force dissipation occurred rapidly and no significant changes in distribution were observed past 6s. Movies showing simulation trajectories can be found in the Supplementary Materials.

with a max peak of 540pN. These bonds had short lifetimes and dissociated quickly, allowing the model to dissipate the contraction and reach equilibrium just before the 6s mark. After this point, the mean force was 11.5pN on average with the max forces averaging 168.3pN. While the equilibrium forces were closer to the 1-38pN range that has been observed *in vitro*[21,35,36], the model's largest forces have not been measured experimentally; peak single $\alpha_5\beta_1$-FN rupture forces measured via AFM were 120pN[20].

The baseline simulation provided a control to test against our two simulation conditions derived from the 1 nm/ns MD simulation. We defined a varying, MD-driven $\alpha_5\beta_1$-FN stiffness as the entire 1nm/ns force-extension curve fit. To evaluate how the nonlinearity of the MD-driven integrin spring affected whole-cell adhesion dynamics, we used the slope of the first segment, 31pN/nm, to define a constant $\alpha_5\beta_1$-FN stiffness test condition.

Overall, the $\alpha_5\beta_1$-FN bond concentration for the constant and MD-driven $\alpha_5\beta_1$-FN stiffness conditions followed a similar trend and were both slower to distribute the contraction load (Fig. 7). For both cases, integrin bond concentrations and forces were situated along the cell border and slowly dissipated the constant applied contractility across the cell surface over time (Fig. 8). Force per integrin for the MD-driven condition was the lowest out of all three simulations with the max and average max forces reaching 33.5 and 2.7pN, respectively. These values were less than the observed 38.9 and 9.7pN max and average max forces observed in the constant 31pN/nm stiffness case. Interestingly, both models aligned with past *in situ* rupture forces of 34 and 38.6pN for $\alpha_5\beta_1$-

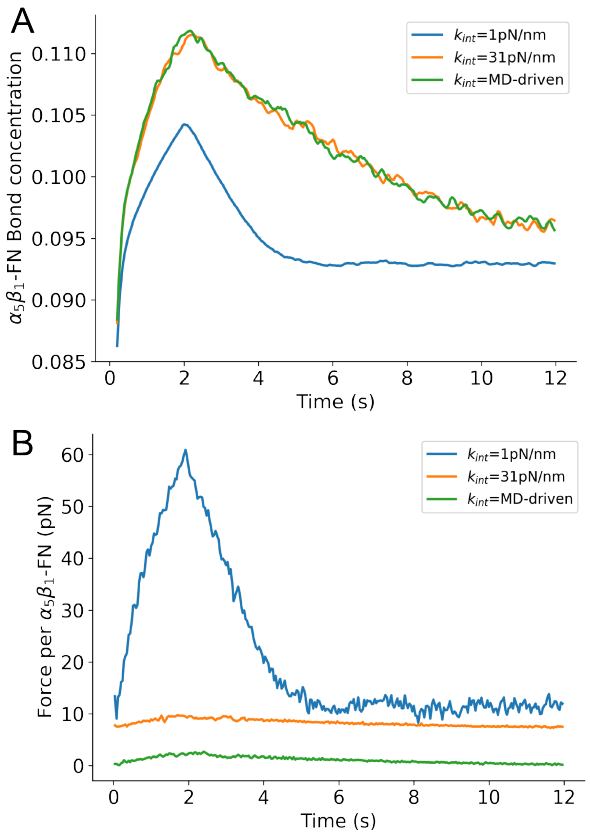


FIG. 7. Whole-cell average A) $\alpha_5\beta_1$-FN bond concentration and B) force per $\alpha_5\beta_1$-FN over the simulation run. Three test conditions for $\alpha_5\beta_1$-FN stiffness are shown per plot: 1) constant 1pN/nm baseline from past models[27,28,34], 2) constant 31pN/nm based on the first segment of the 1nm/ns force-extension curve fit, and 3) MD-driven stiffness derived from using all segments of the curve fit.

FN[35,36] and 40pN for another subtype, $\alpha_V\beta_3$[39]. Chang et al. used FRET-based sensors to measure adhesion forces between 1-7 pN on fibroblasts[21]. Recent work has used leveraged tension gauge tethers to measure single molecule forces on RGD-binding integrins and showed that integrin activation occurs below 12 pN and $\alpha_V\beta_1$ could sustain forces over 54pN in mature FAs[40]. In summary, the models we present showed estimations within reasonable bounds of biophysical forces felt by integrin.

The varying $\alpha_5\beta_1$-FN stiffness of the MD-driven case led to a reduction in the force carried per integrin compared to the constant 31pN/nm case, while having similar bond concentrations over time. This could be due to the sharp increase in $\alpha_5\beta_1$-FN stiffness from 31pN/nm in the first segment to 99.5pN/nm in the second segment of the 1nm/ns force-extension curve (Fig. 2A). The jump in stiffness could have created a larger energetic barrier for the cell contraction to overcome,

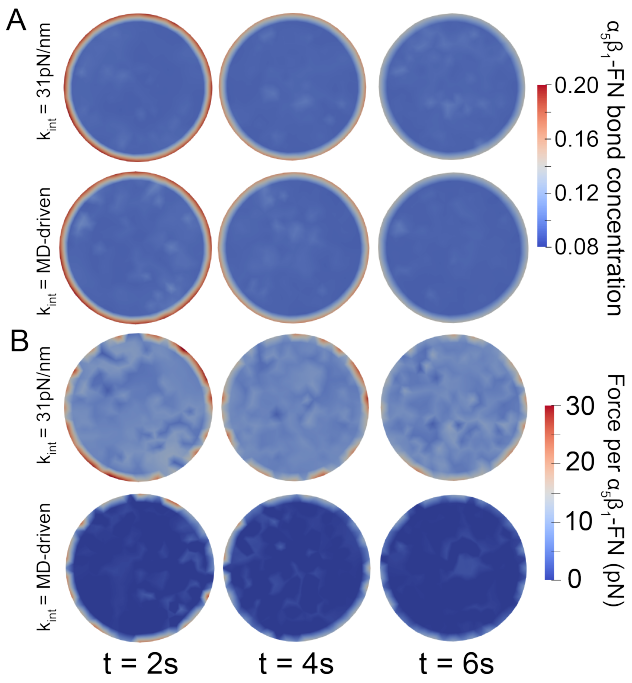


FIG. 8. Whole-cell simulation results for the constant and MD-driven spring stiffnesses. A) $\alpha_5\beta_1$-FN bond concentration and B) Force per $\alpha_5\beta_1$ integrin at three time frames within the first 6s of the simulation. Dissipation continued past 6s, but the changes were minor. Movies showing simulations can be found in the Supplementary Materials.

potentially reducing the force applied to each integrin spring.

## IV. CONCLUSION

We developed a coupled multiscale model which showed how amino acid interactions at the synergy site in FN contribute to the nonlinear force-extension behavior of $\alpha_5\beta_1$-FN, which leads to unique whole-cell adhesion force landscapes. The model demonstrated whole-cell integrin spatial distribution along the cell membrane, consistent with fibroblasts plated *in vitro*[22] and forces within the 120pN maximum single molecule rupture force and 1-38 pN *in situ* rupture forces[21,35,36].

This study has limitations. We used high pull rates in the MD simulations to maintain reasonable computational runtimes. However, this led to large forces during $\alpha_5\beta_1$-FN extension. While the computational cost is a common drawback of MD, the detailed data and outputs gained from the amino acid dynamics and their connection to whole-cell integrin dynamics would have been otherwise unobservable. Therefore, we believe that it was useful to include this demanding

piece of the multiscale model. A combination of slower pull rates and coarse grained MD simulations could be the compromise necessary to investigate the nonlinear mechanics while maintaining some nanoscale details. Also, we chose $\alpha_5\beta_1$ integrin as the sole surface receptor, but cells have additional subtypes with varying roles[34,41] and potentially different adhesion strengths[40]. More investigation is needed to evaluate how $\alpha_5\beta_1$ collaborates with other integrins to manage cell adhesion dynamics.

Our model focused on cell adhesion mechanics and has the potential to grow into a framework that can investigate cell mechanotransduction across multiple scales. For example, we could test how unique mutations on integrins affect whole-cell dynamics *in silico*. Additionally, by incorporating the cell nucleus, we could support early evidence to show how its mechanosensitive nature and material properties could govern gene transcription[42–44]. Key components that have previously been modeled such as the cell membrane, integrin's transmembrane domain, and integrin clustering and diffusion[28,34,45–47] were omitted from our model for simplicity, but could be added as new multiscale mechanobiological questions are posed regarding their mechanics. Lastly, our multiscale framework could be broadened to reveal the nano- and micro- mechanics within nascent engineered tissues and organ-chips that apply controllable biophysical loads at the cell membrane[48–53].

## SUPPLEMENTARY MATERIAL

- Steered MD: `https://github.com/dredremontes/pull_integrinMD`
- Whole-cell: `https://github.com/dredremontes/wholeCellFE`
- Finite Element (Whole-cell) Model Equations
- Table S1: Energy Minimization Parameters
- Table S2: NVT Parameters
- Table S3: NPT Parameters
- Table S4: Steered MD Parameters
- Table S5: Force Distribution Analysis Parameters
- Table S6: Whole-cell model parameters
- Fig. S1: Energy Minimization and NVT RMSD

- Fig. S2: NPT RMSD, Pressure, and Temperature
- Movie S1: 1nm/ns extension of $\alpha_5\beta_1$-FN
- Movie S2: 10nm/ns extension of $\alpha_5\beta_1$-FN
- Movie S3: 1nm/ns Force Distribution Analysis
- Movie S4: 10nm/ns Force Distribution Analysis
- Movie S5: All Whole-cell simulations

## AUTHOR CONTRIBUTIONS

**A.R. Montes**: Conceptualization, data curation, formal analysis, funding acquisition, investigation, methodology, project administration, software, validation, visualization, and writing - original. **G. Gutierrez**: Formal analysis, investigation. **A.B. Tepole**: Conceptualization, data curation, formal analysis, funding acquisition, investigation, methodology, project administration, resources, software, supervision, validation, visualization, writing - original, and writing - review & editing. **M.R.K. Mofrad**: Conceptualization, funding acquisition, project administration, resources, supervision, and writing - review & editing.

## ACKNOWLEDGMENTS

This research used Stampede2 at Texas Advanced Computing Center through allocation MCB100146 from Advanced Cyberinfrastructure Coordination Ecosystem: Services & Support (ACCESS) super-computing facilities, supported by the National Science Foundation grants #2138259, #2138286, #2138307, #2137603, and #2138296. A.R.M. was funded by the Ford Foundation's Predoctoral Fellowship awarded by the National Academies of Science, Engineering, and Medicine and the Robert N. Noyce Fellowship from UC Berkeley's College of Engineering. G.G. was supported by the National Science Foundation California Alliance for Minority Participation. Thank you to Ghafar Yerima and Nya Domkam for helping set up GROMACS and gromacs-fda. We also thank the Molecular Cell Biomechanics Lab and the Berkeley Biomechanics Lab for fruitful discussions that improved the manuscript.

## DATA AVAILABILITY STATEMENT

The data that support the findings of this study are available from the corresponding author upon reasonable request.

## CONFLICTS OF INTEREST

There are no conflicts to disclose.

## REFERENCES

## REFERENCES

[1]D. E. Ingber, "Mechanosensation through integrins: cells act locally but think globally," Proceedings of the National Academy of Sciences **100**, 1472–1474 (2003).

[2]Z. Jahed, H. Shams, M. Mehrbod, and M. R. Mofrad, "Mechanotransduction pathways linking the extracellular matrix to the nucleus," International review of cell and molecular biology **310**, 171–220 (2014).

[3]J. Zhu, C. V. Carman, M. Kim, M. Shimaoka, T. A. Springer, and B.-H. Luo, "Requirement of $\alpha$ and $\beta$ subunit transmembrane helix separation for integrin outside-in signaling," Blood, The Journal of the American Society of Hematology **110**, 2475–2483 (2007).

[4]P. E. Hughes, F. Diaz-Gonzalez, L. Leong, C. Wu, J. A. McDonald, S. J. Shattil, and M. H. Ginsberg, "Breaking the integrin hinge: A defined structural constraint regulates integrin signaling," Journal of Biological Chemistry **271**, 6571–6574 (1996).

[5]E. Puklin-Faucher and M. P. Sheetz, "The mechanical integrin cycle," Journal of cell science **122**, 179–186 (2009).

[6]J. Takagi, B. M. Petre, T. Walz, and T. A. Springer, "Global conformational rearrangements in integrin extracellular domains in outside-in and inside-out signaling," Cell **110**, 599–611 (2002).

[7]S. W. Moore, P. Roca-Cusachs, and M. P. Sheetz, "Stretchy proteins on stretchy substrates: the important elements of integrin-mediated rigidity sensing," Developmental cell **19**, 194–206 (2010).

[8]J. Deng, C. Zhao, J. P. Spatz, and Q. Wei, "Nanopatterned adhesive, stretchable hydrogel to control ligand spacing and regulate cell spreading and migration," ACS nano **11**, 8282–8291 (2017).

[9]J. Lee, A. A. Abdeen, D. Zhang, and K. A. Kilian, "Directing stem cell fate on hydrogel substrates by controlling cell geometry, matrix mechanics and adhesion ligand composition," Biomaterials **34**, 8140–8148 (2013).

[10]P. Moreno-Layseca, J. Icha, H. Hamidi, and J. Ivaska, "Integrin trafficking in cells and tissues," Nature cell biology **21**, 122–132 (2019).

[11]J. Takagi, K. Strokovich, T. A. Springer, and T. Walz, "Structure of integrin $\alpha 5\beta 1$ in complex with fibronectin," The EMBO journal **22**, 4607–4615 (2003).

[12]S. Schumacher, D. Dedden, R. V. Nunez, K. Matoba, J. Takagi, C. Biertümpfel, and N. Mizuno, "Structural insights into integrin $\alpha 5\beta 1$ opening by fibronectin ligand," Science Advances **7**, eabe9716 (2021).

[13]T. Nagai, N. Yamakawa, S.-i. Aota, S. S. Yamada, S. K. Akiyama, K. Olden, and K. M. Yamada, "Monoclonal antibody characterization of two distant sites required for function of the central cell-binding domain of fibronectin in cell adhesion, cell migration, and matrix assembly." The Journal of cell biology **114**, 1295–1305 (1991).

[14]I. Wierzbicka-Patynowski and J. E. Schwarzbauer, "The ins and outs of fibronectin matrix assembly," Journal of cell science **116**, 3269–3276 (2003).

[15]J. C. Friedland, M. H. Lee, and D. Boettiger, "Mechanically activated integrin switch controls $\alpha 5\beta 1$ function," Science **323**, 642–644 (2009).

[16]D. Barkan, L. H. El Touny, A. M. Michalowski, J. A. Smith, I. Chu, A. S. Davis, J. D. Webster, S. Hoover, R. M. Simpson, J. Gauldie, *et al.*, "Metastatic growth from dormant cells induced by a col-i–enriched fibrotic environment metastatic outgrowth from dormant tumor cells," Cancer research **70**, 5706–5716 (2010).

[17]J. Z. Kechagia, J. Ivaska, and P. Roca-Cusachs, "Integrins as biomechanical sensors of the microenvironment," Nature Reviews Molecular Cell Biology **20**, 457–473 (2019).

[18]M. J. Paszek, N. Zahir, K. R. Johnson, J. N. Lakins, G. I. Rozenberg, A. Gefen, C. A. Reinhart-King, S. S. Margulies, M. Dembo, D. Boettiger, *et al.*, "Tensional homeostasis and the malignant phenotype," Cancer cell **8**, 241–254 (2005).

[19]J. J. Northey, L. Przybyla, and V. M. Weaver, "Tissue force programs cell fate and tumor aggression mechanotransduction in cell fate and cancer aggression," Cancer discovery **7**, 1224–1237

(2017).

[20]F. Li, S. D. Redick, H. P. Erickson, and V. T. Moy, "Force measurements of the $\alpha 5\beta 1$ integrin–fibronectin interaction," Biophysical journal **84**, 1252–1262 (2003).

[21]A. C. Chang, A. H. Mekhdjian, M. Morimatsu, A. K. Denisin, B. L. Pruitt, and A. R. Dunn, "Single molecule force measurements in living cells reveal a minimally tensioned integrin state," ACS nano **10**, 10745–10752 (2016).

[22]M. Benito-Jardon, S. Klapproth, I. Gimeno-LLuch, T. Petzold, M. Bharadwaj, D. J. Müller, G. Zuchtriegel, C. A. Reichel, and M. Costell, "The fibronectin synergy site re-enforces cell adhesion and mediates a crosstalk between integrin classes," Elife **6**, e22264 (2017).

[23]L. Schrödinger, "The PyMOL molecular graphics system, version 1.8," (2015).

[24]M. J. Abraham, T. Murtola, R. Schulz, S. Páll, J. C. Smith, B. Hess, and E. Lindahl, "Gromacs: High performance molecular simulations through multi-level parallelism from laptops to supercomputers," SoftwareX **1**, 19–25 (2015).

[25]W. Humphrey, A. Dalke, and K. Schulten, "VMD – Visual Molecular Dynamics," Journal of Molecular Graphics **14**, 33–38 (1996).

[26]L. Treloar, "The elasticity and related properties of rubbers," Reports on progress in physics **36**, 755 (1973).

[27]Y. Guo, S. Calve, and A. B. Tepole, "Multiscale mechanobiology: Coupling models of adhesion kinetics and nonlinear tissue mechanics," Biophysical Journal **121**, 525–539 (2022).

[28]B. Cheng, W. Wan, G. Huang, Y. Li, G. M. Genin, M. R. Mofrad, T. J. Lu, F. Xu, and M. Lin, "Nanoscale integrin cluster dynamics controls cellular mechanosensing via faky397 phosphorylation," Science advances **6**, eaax1909 (2020).

[29]T. Brochu and R. Bridson, "Robust topological operations for dynamic explicit surfaces," SIAM Journal on Scientific Computing **31**, 2472–2493 (2009).

[30]W. Chen, J. Lou, J. Hsin, K. Schulten, S. C. Harvey, and C. Zhu, "Molecular dynamics simulations of forced unbending of integrin $\alpha$v$\beta$3," PLoS computational biology **7**, e1001086 (2011).

[31]M. Kulke and W. Langel, "Molecular dynamics simulations to the bidirectional adhesion signaling pathway of integrin $\alpha$v$\beta$3," Proteins: Structure, Function, and Bioinformatics **88**, 679–688 (2020).

[32]M. Gao, D. Craig, V. Vogel, and K. Schulten, "Identifying unfolding intermediates of fn-iii10 by steered molecular dynamics," Journal of molecular biology **323**, 939–950 (2002).

[33]A. R. Bausch, F. Ziemann, A. A. Boulbitch, K. Jacobson, and E. Sackmann, "Local measurements of viscoelastic parameters of adherent cell surfaces by magnetic bead microrheometry," Biophysical journal **75**, 2038–2049 (1998).

[34]T. C. Bidone, A. V. Skeeters, P. W. Oakes, and G. A. Voth, "Multiscale model of integrin adhesion assembly," PLOS Computational Biology **15**, e1007077 (2019).

[35]A. Trache, J. P. Trzeciakowski, L. Gardiner, Z. Sun, M. Muthuchamy, M. Guo, S. Y. Yuan, and G. A. Meininger, "Histamine effects on endothelial cell fibronectin interaction studied by atomic force microscopy," Biophysical journal **89**, 2888–2898 (2005).

[36]X. Wu, Z. Sun, A. Foskett, J. P. Trzeciakowski, G. A. Meininger, and M. Muthuchamy, "Cardiomyocyte contractile status is associated with differences in fibronectin and integrin interactions," American Journal of Physiology-Heart and Circulatory Physiology **298**, H2071–H2081 (2010).

[37]P. Roca-Cusachs, T. Iskratsch, and M. P. Sheetz, "Finding the weakest link–exploring integrin-mediated mechanical molecular pathways," Journal of cell science **125**, 3025–3038 (2012).

[38]A. F. Oberhauser, C. Badilla-Fernandez, M. Carrion-Vazquez, and J. M. Fernandez, "The mechanical hierarchies of fibronectin observed with single-molecule afm," Journal of molecular biology **319**, 433–447 (2002).

[39]X. Wang and T. Ha, "Defining single molecular forces required to activate integrin and notch signaling," Science **340**, 991–994 (2013).

[40]M. H. Jo, J. Li, V. Jaumouillé, Y. Hao, J. Coppola, J. Yan, C. M. Waterman, T. A. Springer, and T. Ha, "Single-molecule characterization of subtype-specific $\beta 1$ integrin mechanics," Nature communications **13**, 7471 (2022).

[41]J. L. Young, X. Hua, H. Somsel, F. Reichart, H. Kessler, and J. P. Spatz, "Integrin subtypes and nanoscale ligand presentation influence drug sensitivity in cancer cells," Nano Letters **20**, 1183–1191 (2020).

[42]N. Wang, J. D. Tytell, and D. E. Ingber, "Mechanotransduction at a distance: mechanically coupling the extracellular matrix with the nucleus," Nature reviews Molecular cell biology **10**, 75–82 (2009).

[43]S. Wang, E. Stoops, U. Cp, B. Markus, A. Reuveny, E. Ordan, and T. Volk, "Mechanotransduction via the linc complex regulates dna replication in myonuclei," Journal of Cell Biology **217**, 2005–2018 (2018).

[44]S. Tsukamoto, T. Asakawa, S. Kimura, N. Takesue, M. R. Mofrad, and N. Sakamoto, "Intranuclear strain in living cells subjected to substrate stretching: A combined experimental and computational study," Journal of Biomechanics **119**, 110292 (2021).

[45]M. J. Paszek, D. Boettiger, V. M. Weaver, and D. A. Hammer, "Integrin clustering is driven by mechanical resistance from the glycocalyx and the substrate," PLoS computational biology **5**, e1000604 (2009).

[46]M. Mehrbod and M. R. Mofrad, "Localized lipid packing of transmembrane domains impedes integrin clustering," PLoS computational biology **9**, e1002948 (2013).

[47]M. Mehrbod, S. Trisno, and M. R. Mofrad, "On the activation of integrin $\alpha$iib$\beta$3: outside-in and inside-out pathways," Biophysical journal **105**, 1304–1315 (2013).

[48]A. Elosegui-Artola, A. Gupta, A. J. Najibi, B. R. Seo, R. Garry, C. M. Tringides, I. de Lázaro, M. Darnell, W. Gu, Q. Zhou, *et al.*, "Matrix viscoelasticity controls spatiotemporal tissue organization," Nature Materials , 1–11 (2022).

[49]G. R. López-Marcial, A. Y. Zeng, C. Osuna, J. Dennis, J. M. García, and G. D. O'Connell, "Agarose-based hydrogels as suitable bioprinting materials for tissue engineering," ACS Biomaterials Science & Engineering **4**, 3610–3616 (2018).

[50]J. P. McKinley, A. R. Montes, M. N. Wang, A. R. Kamath, G. Jimenez, J. Lim, S. A. Marathe, M. R. Mofrad, and G. D. O'Connell, "Design of a flexing organ-chip to model in situ loading of the intervertebral disc," Biomicrofluidics **16**, 054111 (2022).

[51]J. E. Barthold, B. M. St. Martin, S. L. Sridhar, F. Vernerey, S. E. Schneider, A. Wacquez, V. L. Ferguson, S. Calve, and C. P. Neu, "Recellularization and integration of dense extracellular matrix by percolation of tissue microparticles," Advanced functional materials **31**, 2103355 (2021).

[52]P. Dhavalikar, A. Robinson, Z. Lan, D. Jenkins, M. Chwatko, K. Salhadar, A. Jose, R. Kar, E. Shoga, A. Kannapiran, *et al.*, "Review of integrin-targeting biomaterials in tissue engineering," Advanced healthcare materials **9**, 2000795 (2020).

[53]A. Sontheimer-Phelps, B. A. Hassell, and D. E. Ingber, "Modelling cancer in microfluidic human organs-on-chips," Nature Reviews Cancer **19**, 65–81 (2019).